

# Reanalysis of the near-infrared extragalactic background light based on the IRTS observations

T. Matsumoto<sup>1</sup>

Institute of Astronomy and Astrophysics, Academia Sinica, Taipei 10617, Taiwan

M. G. Kim

Seoul National University, Seoul 151-742, Korea

J. Pyo

Korea Astronomy and Space Science Institute, Daejeon 305-348, Korea

and

K. Tsumura

Frontier Research Institute for Interdisciplinary Science, Tohoku University, Sendai, Miyagi  
980-8578, Japan

Received \_\_\_\_\_; accepted \_\_\_\_\_

---

<sup>1</sup>Institute of Space and Astronautical Science, Japan Aerospace Exploration Agency,  
Kanagawa 252-5210, Japan

## ABSTRACT

We reanalyze data of near-infrared background taken by Infrared Telescope in Space (IRTS) based on up-to-date observational results of zodiacal light, integrated star light and diffuse Galactic light. We confirm the existence of residual isotropic emission, which is slightly lower but almost the same as previously reported. At wavelengths longer than  $2\ \mu\text{m}$ , the result is fairly consistent with the recent observation with AKARI. We also perform the same analysis using a different zodiacal light model by Wright and detected residual isotropic emission that is slightly lower than that based on the original Kelsall model. Both models show the residual isotropic emission that is significantly brighter than the integrated light of galaxies.

*Subject headings:* cosmology: observations — diffuse radiation — infrared

## 1. Introduction

The extragalactic background light (EBL) has been observed over a wide range of wavelengths to examine the energy density of the universe. In particular, the near-infrared EBL has been thought to provide an important clue to our understanding of the early universe and the evolution of galaxies. The COsmic Background Explorer (COBE) (Cambr sy et al. 2001; Gorjian et al. 2000; Wright and Reese 2000; Levenson et al. 2007) and the InfraRed Telescope in Space (IRTS) (Matsumoto et al. (2005), hereafter referred to as paper I) discovered that a significant fraction of the near-infrared isotropic emission cannot be explained with known foreground emission. Recent AKARI observations (Tsumura et al. 2013d) also show a consistent result with COBE and IRTS at wavelengths longer than  $2\ \mu\text{m}$ . This excess background emission in the near-infrared sky is particularly interesting in light of the recent discovery of large excess fluctuation of the near-infrared sky (Kashlinsky et al. 2005, 2007a,b; Matsumoto et al. 2011; Zemcov et al. 2014).

The results of paper I attracted wide interest due to the high accuracy enabled by the unique low resolution spectroscopy of IRTS, and its point source detection limit ( $\sim 11$  mag) which was much deeper than COBE. However, as Mattila (2006) pointed out, paper I did not take the contribution of the diffuse Galactic light (DGL) into account. Uncertainty of the zodiacal light (ZL) model has been also raised, since ZL is the dominant foreground emission with a spectrum similar to the residual isotropic emission (Dwek et al. 2005).

In response to these concerns, we decided to reanalyze the IRTS data using up-to-date observations of ZL, integrated star light (ISL), and DGL. While in paper I, we adopted the Kelsall et al. (1998) ZL model, in this work, we perform the same analysis using a different ZL model (the so called Wright model, Wright (1998)), and examine the difference between two models.

The overall outline of the paper is as follows. In section 1, we briefly present the IRTS

observation and the acquisition of raw data in section 2. In section 3, we estimate the contribution of foreground emission, ZL, ISL and DGL based on the latest observations. In section 4, we search for the residual isotropic emission for two ZL models based on the correlation with the sky brightness after subtracting the ISL and DGL. Finally, in section 5, we discuss the astrophysical implications of the detected excess brightness.

## 2. IRTS observations

We now give a brief description of the IRTS mission and the data acquisition process. Details of IRTS mission can be found in paper I.

IRTS was one of the mission experiments on the small space platform, Space Flyer Unit (SFU), that was launched on March 18, 1995. On a low-inclination near-earth orbit, IRTS continuously surveyed the sky avoiding both the sun and the earth. IRTS observations lasted for about 30 days, during which 7% of the sky was surveyed (Murakami et al. 1996).

The Near InfraRed Spectrometer (NIRS) is one of the focal plane instruments of IRTS, and was optimized to obtain spectra of the diffuse background (Noda et al. 1994). Details of the flight performance of NIRS can be found in Noda et al. (1996). NIRS covered a wavelength range from 1.4  $\mu\text{m}$  to 4.0  $\mu\text{m}$ s with a spectral resolution of 0.13  $\mu\text{m}$ , providing 24 independent wavelength bands. The beam size was 8 arcmin square and the detection limit for point sources was  $\sim 11$  mag, and both are considerably better than those of COBE. The limiting magnitudes at wavelengths shorter and longer than 2.5  $\mu\text{m}$  are dominated by the sky fluctuation and readout noise, respectively (Noda et al. (1996), paper I).

The NIRS detectors were of the charge integrating type and the ramp curves with one cycle of 65.54 sec were sent to the ground for all of the 24 wavelength bands. We retrieved the signal of the sky using 5 sec integration times (i.e. the signal difference in 5 sec in ramp

curve), during which no distinguishable stars and no cosmic ray hits were detected in any band. We obtained signals of the sky brightness after subtracting the dark current when the cold shutter was closed. During each 5 sec integration, the telescope axis moved about 20 arcmin along a great circle, resulting in a trapezoidal beam pattern,  $8 \text{ arcmin} \times 20 \text{ arcmin}$  in area. To make the contribution of stars and Galactic emission less effective, high Galactic latitude ( $b > 40^\circ$ ) data were extracted from the full data set for the background radiation analysis. The highest Galactic latitude was  $58^\circ$ , while the ecliptic latitude ranged from  $12^\circ$  to  $71^\circ$  in the selected sky. Complete spectra of the sky were secured at 1010 fields. Sky coverage of 1010 fields is  $\sim 60\%$  of the surveyed area.

### 3. Foreground emission

#### 3.1. Zodiacal light (ZL)

The zodiacal light (ZL) is the emission component of the solar system which consists of scattered sunlight and thermal emission by interplanetary dust. We adopted the model by Kelsall et al. (1998) in paper I, which is a physical model constructed using the seasonal variation of the ZL observed with the Diffuse InfraRed Background Explorer (DIRBE) on COBE. At the same time, Wright (1998) proposed a different physical model based on the so called "strong zodi principle" assuming no residual emission at  $25 \mu\text{m}$  towards the ecliptic pole. In this paper, we use both models and examine the difference of residual isotropic emission. As for the Wright model, we used the model revised by Gorjian et al. (2000).

We retrieve the brightness of the ZL in the DIRBE bands corresponding to the 1010 IRTS fields at the epoch of the IRTS observations for both models, and construct the ZL model brightness for the IRTS bands. We obtain the model spectrum for the scattering

and thermal emission part, separately. For the scattering part, we simply normalize the spectral shape of the sun (ASTM G173-03 Reference System)<sup>1</sup> at the K band model brightness. For the thermal part, we extrapolate the M band model brightness to the shorter IRTS wavelengths, assuming a 300K blackbody in accordance with recent AKARI observations (Tsumura et al. 2013b). The ZL model spectrum is obtained by summing the scattering part with the thermal emission part. Compared to the model used in paper I, the ZL component at wavelengths longer than  $3\ \mu\text{m}$  is slightly brighter. In the L band, our adopted models render a  $\sim 6\%$  brighter value than the original model, but still within the uncertainty of the models. The validity of the adopted ZL spectrum will be compared with observations in section 4.

### 3.2. Integrated star light (ISL)

The integrated star light (ISL) for stars fainter than the limiting magnitude composes a portion of the foreground emission. The best way to estimate the ISL is to sum the brightness of stars in the 2MASS catalog that fall within the beam, however, the uncertainty of the attitude determination and irregular beam pattern elongated along scan path makes this analysis difficult. While, in paper I, we applied the SKY model (Cohen 1997), and assume a simple  $\text{cosec}(b)$  law to the model ISL at three selected fields, in this paper, we obtain the model ISL based on an improved model, that is, the TRILEGAL Galaxy model (Girardi et al. 2005). We further calculate ISL for 12 equally-spaced fields along the scan path for the I, J, H,  $K_S$ , L, and  $L_S$  bands.

Since the fluctuation of the ISL is not negligible, we perform 50 Monte-Carlo simulations

---

<sup>1</sup>Available in electronic form at  
<http://rredc.nrel.gov/solar/spectra/am1.5/astmg173/astmg173.html>

for a 1 square degree field for all TRILEGAL stars fainter than the IRTS limiting magnitude and assign their average values to be the TRILEGAL ISL. However, the overall uncertainty of the TRILEGAL model is so large, that we must calibrate the TRILEGAL ISL by comparing with the 2MASS ISL for the H and K bands. The 2MASS ISL is obtained by summing the ISL for the 2MASS stars fainter than the IRTS limiting magnitudes, and that for stars fainter than 2MASS limiting magnitudes (15.8 mag for the J band and 15.1 mag for the H band; Skrutskie et al. (2006)) which is estimated by adopting the TRILEGAL model. Contribution of the latter part to the 2MASS ISL is only a few percent. Fig.1 shows the correlation between the TRILEGAL ISL and the 2MASS ISL for the 12 selected fields. Left and right panels indicate the results for the H and K bands, respectively. Horizontal errors in Fig.1 represent the  $1\sigma$  dispersion of the TRILEGAL ISL as a result of these Monte-Carlo simulations and indicate the expected fluctuation of TRILEGAL ISL. Fig.1 clearly indicates that the 2MASS ISL is brighter than the TRILEGAL ISL both for the H and K bands, and the scatter of the 2MASS ISL is consistent with that expected from the TRILEGAL model. Based on this analysis, we finally obtain the model ISL by multiplying TRILEGAL ISL by 1.23 with 8 % error. The ISL for the 1010 fields observed with IRTS was obtained by interpolating the two neighboring model fields assuming a  $\text{cosec}(b)$  law. The ISL for 24 of the IRTS bands was estimated by interpolating the model ISL using the blackbody spectrum with the same limiting magnitudes as in paper I.

Besides the model errors, we calculate the model ISL for variation of  $\pm 0.5$  mag in the limiting magnitude and assigned the difference to be peak-to-peak errors. This error is a little lower than the error due to uncertainty of the model ISL. The model ISL thus obtained renders a more reliable brightness and spatial distribution than that of paper I.

### 3.3. Diffuse Galactic

light (DGL) The DGL was not taken into account in paper I as a foreground emission, as mentioned in Mattila (2006), since no reliable observation of DGL was reported at that time and the contribution of DGL to the overall sky brightness was thought to be small. Recently new observations of the near-infrared DGL have been attained, and we attempt to estimate the DGL for the IRTS fields and bands. Tsumura et al. (2013c) obtained low resolution spectra of the diffuse sky with AKARI for the wavelengths ranging from  $2\ \mu\text{m}$  to  $5\ \mu\text{m}$ , detecting a clear correlation between the near-infrared sky brightness and the far-infrared emission ( $100\ \mu\text{m}$ , Schlegel et al. (1998)). A PAH band at  $3.3\ \mu\text{m}$  was clearly detected, however, the detection was limited to the Galactic plane at  $b < 15^\circ$ . Arai et al. (2015) performed a similar correlation analysis with data from the Low Resolution Spectrometer (LRS) (Tsumura et al. 2013a), one of the instruments on the sounding rocket experiment, CIBER (Cosmic Infrared Background ExpeRiment, Zemcov et al. (2013)). They also detected a clear correlation with the far-infrared emission for the wavelength range from  $0.95\ \mu\text{m}$  to  $1.65\ \mu\text{m}$  at high Galactic latitudes.

Fig.2 summarizes their results. The ratio of the DGL to the far-infrared ( $100\ \mu\text{m}$ ) emission is shown in units of  $\text{nWm}^{-2}\text{sr}^{-1} / \mu\text{Wm}^{-2}\text{sr}^{-1}$ . Filled and open circles represent the result of CIBER and AKARI, respectively. The CIBER result indicates scattered star light by interstellar dust, and the AKARI result shows the thermal emission of the fine dust particles transiently heated by a single UV photon. We fit the scattered part with the ZDA04-BC03 (Brandt and Draine 2012) model recommended by Arai et al. (2015), as is shown with the dotted line. As for the thermal part, it is not clear that the AKARI result can be applied to the DGL at high Galactic latitudes, since Tsumura et al. (2013c) reported lower level of thermal DGL than expected from Fig.2 at higher Galactic latitudes. Therefore, we first assume that no thermal part exists at IRTS fields where Galactic



latitudes are higher than  $40^\circ$ . The thermal contribution, especially from the  $3.3\ \mu\text{m}$  PAH feature will be discussed again in section 4. Adopted values for IRTS bands are shown by open squares in Fig.2 for which an error of  $\pm 20\%$  was applied.

We used the far-infrared map compiled by Schlegel et al. (1998), and retrieved  $100\ \mu\text{m}$  brightness for a 12 arcmin diameter FOV for the 1010 IRTS fields. Using the ratio of the DGL to the  $100\ \mu\text{m}$  brightness (Fig.2), we are able to obtain DGL for 24 IRTS bands and for 1010 IRTS fields.

#### 4. Residual isotropic emission

We attempt to obtain the residual isotropic emission with same procedure as paper I. First, we subtract the ISL and DGL from the observed sky brightness and make a correlation analysis with the model ZL brightness. The upper sets of data points in Fig.3 show typical correlation diagrams at  $1.8\ \mu\text{m}$  both for the Kelsall model (left panel) and the Wright model (right panel). For both models, we find an excellent linear correlation for all wavelength bands, and intersection of linear fit line at  $x = 0$  provides the residual isotropic emission. The lower sets of data points in Fig.3 show the individual residual emission for the 1010 IRTS fields at  $1.8\ \mu\text{m}$  after subtracting all foreground emission components, demonstrating that the residual emission is fairly isotropic. Since error levels are almost same for two models, it must be noted that there is no clear preference between these two models.

Fig.4 shows the dependence of the residual emission at  $1.8\ \mu\text{m}$  on the Galactic latitudes for the case of the Kelsall model. Data points indicate averaged values for 10 degrees along the Galactic longitude. Filled circles and open circles indicate the result of present work and that of paper I, respectively. The large scale structure observed in paper I disappeared,

and the data points of the present work show random scatter. This improvement is mainly due to our revision of the ISL model.

Fig.5 shows slopes of the linear fit line both for the Kelsall and Wright model. In both models, slopes are a few percent larger than 1.0, which is consistent with paper I. We regard this as the deviation of the ZL spectrum from the solar spectrum which reflects the physical properties of interplanetary dust. The ZL spectrum can be obtained by multiplying the solar spectrum by these values, showing reddening of the ZL color at near-infrared wavelengths. The observed spectrum smoothly connects to the ZL spectrum from 0.75 to 1.6  $\mu\text{m}$  observed with CIBER and is consistent with the J band brightness of the Kelsall model based on the DIRBE data (see Fig. 9 in Tsumura et al. (2010)).

Fig.6 shows the residual isotropic emission obtained for both the Kelsall and Wright model, with two different sets of error bars. The inner and outer error bars indicate the random and total error, respectively. Aside from the random error, the systematic error makes the spectrum change in the same direction. Random errors include: fitting errors from correlation analysis, ISL errors due to limiting magnitudes, calibration errors, and DGL errors. Systematic errors are due to model errors of ZL and ISL. As paper I, errors in the ZL model are estimated by interpolating the uncertainties in the original model (Table 7 in Kelsall et al. (1998)). ZL model error is the dominant source of error and amounts to  $\sim 80\%$  of total error. Table 1 indicates numerical values for the residual emission and their error for two models.

Compared with residual emission in paper I, which is based on the Kelsall model, the peak brightness of the residual emission of the present work is  $\sim 11 \text{ nWm}^{-2}\text{sr}^{-1}$  lower. The residual emission at wavelengths longer than 2  $\mu\text{m}$  is almost the same as that of paper I. A flat spectrum for the three shortest wavelength bands is a characteristic feature found in this analysis. The residual emission obtained by adopting the Wright model for the ZL

provides  $\sim 7 \text{ nWm}^{-2}\text{sr}^{-1}$  lower peak value than that obtained by adopting the Kelsall model but the spectral shape is very similar to each other. Fig.6 implies that there exists excess near-infrared isotropic residual emission independent of the choice of the two ZL models used here.

Additionally, we make the same analysis including the thermal part of the DGL. In this case, residual emission at  $3.28 \mu\text{m}$  PAH feature is estimated to be  $\sim 20 \%$  ( $\sim 2.6 \text{ nWm}^{-2}\text{sr}^{-1}$ ) lower than that of Fig.6, causing a sharp absorbing feature in the spectrum of the residual emission. We also find that the sky brightness at  $3.28 \mu\text{m}$  after subtracting ZL and ISL shows no correlation with far-infrared sky brightness. These results favor the non-existence of the PAH feature at high Galactic latitudes, however, this is not conclusive given that random noise at  $3.28 \mu\text{m}$  is so large. In any case, the contribution of the thermal part of DGL is almost negligible and does not significantly change the final result.

Fig.7 shows the breakdown of the emission components whose spectra are obtained as the average brightness at high ecliptic latitudes ( $\beta > 70^\circ$ ) and high Galactic latitudes ( $b > 45^\circ$ ) for the case of the Kelsall model. The ZL Spectrum indicated is obtained by applying the result of correlation analysis (Fig.5). The residual isotropic emission amounts to  $\sim 1/4$  of the ZL, and this is comparable with the seasonal variation of the ZL.

Fig.8 summarizes the observations of the residual isotropic emission for which the Kelsall model is applied for the ZL. Typical two observations (Cambr  sy et al. 2001; Levenson et al. 2007) are shown for COBE data. Solid line indicates the model of the integrated light of galaxies (ILG) by Totani and Yoshii (2000), which is consistent with deep Galaxy counts (Keenan et al. 2010). The brightness of this work is a little lower than that in paper I, but still consistent with COBE and AKARI (Tsumura et al. 2013d). It must be emphasized that these three satellite observations render consistent residual emission within error, although the beam size and limiting magnitudes are completely

different. In the optical region, two new observations are plotted. Matsuoka et al. (2011) re-analyzed the Pioneer 10/11 data, where the ZL is negligible near the Jupiter orbit, while Mattila et al. (2011) attempted to detect the EBL using shadowing effect of dark cloud at high Galactic latitude. Both results show that the observed background brightness is consistent with the known foreground emission. On the other hand, HST observations by Bernstein (2007) show fairly bright residual emission at a similar level as this work.

Fig.9 indicates excess brightness over ILG. Since some galaxies are already removed in Bernstein (2007) and Tsumura et al. (2013d), we subtracted 10 and 50 % of the ILG (solid line in Fig. 8) from their data in Fig.8, respectively, based on ILG magnitude relationship by Keenan et al. (2010). We find improved consistency between IRTS and AKARI data. As already mentioned in paper I, the blue Rayleigh-Jeans like spectrum is clearly seen at wavelengths longer than  $1.6 \mu\text{m}$ .

## 5. Discussion

It has been suspected that the residual isotropic emission is a part of the ZL since the spectrum of the residual isotropic emission is similar to that of the ZL (Dwek et al. 2005). However, it is not so easy to construct the new ZL model which includes the residual isotropic emission, since the residual emission is comparable to the seasonal variation of the ZL. One possible approach is to add the new dust component which has a heliocentric and spherically symmetric distribution. It is, however, difficult to maintain the spherically symmetric distribution of interplanetary dust of inner solar system due to the perturbation by planets. Maintaining the supply of dust against Poynting-Robertson drag is also difficult. These considerations imply that the new dust component must be beyond the orbit of Jupiter. If we attribute the residual isotropic emission to the scattered sunlight by interplanetary dust, the brightness extrapolated to visible wavelengths amounts to  $\sim$

$100 \text{ nWm}^{-2}\text{sr}^{-1}$ , assuming a solar spectrum. The existence of such a component, however, is not detected with Pioneer 10/11 observations (Hanner et al. 1974). A recent reanalysis of the Pioneer 10/11 data by Matsuoka et al. (2011) confirms that the residual isotropic emission near the orbit of Jupiter is less than  $10 \text{ nWm}^{-2}\text{sr}^{-1}$  at  $0.44$  and  $0.64 \mu\text{m}$ . These results indicate that the new dust component does not exist, otherwise the new component dust has peculiar optical properties.

The light of the first stars at the re-ionization epoch is another possible emission source which has been thought to be an important clue to delineate the star formation history of the universe. However, recent theoretical works based on high redshift galaxies predict much less contribution of the first stars to the near-infrared background (Cooray et al. 2012b; Yue et al. 2013b).

It has been thought that the spatial fluctuation of the sky directly provides the characteristic feature of the EBL, since the fluctuation of the ZL is so low (Pyo et al. 2012). Large fluctuations at angles larger than  $100 \text{ arcsec}$  that cannot be explained with the known foreground sources are detected with Spitzer at  $3.6$  and  $4.5 \mu\text{m}$  (Kashlinsky et al. 2005, 2007a,b) and AKARI at  $2.4$ ,  $3.6$  and  $4.2 \mu\text{m}$  (Matsumoto et al. 2011). Recent Spitzer (Kashlinsky et al. 2012; Cooray et al. 2012a) and AKARI (Seo et al. 2015) observations confirm that flat fluctuation spectra extend to degree scales. The spectrum of fluctuation is blue Rayleigh-Jeans like (Matsumoto et al. 2011) and clear spatial correlations are found for both AKARI and Spitzer wavelengths.

Zemcov et al. (2014) recently report the result of sounding rocket observations with CIBER. They detect large fluctuation at  $1.1$  and  $1.6 \mu\text{m}$ . In Fig.9 we over-plot the result of Fig.2 in Zemcov et al. (2014) as large filled squares. Unit is shown in right ordinate with same dynamic range as excess brightness. The spectrum of the fluctuations is similar to the excess brightness, suggesting that the excess fluctuation and brightness may be of same

origin. A ratio of the absolute brightness to the fluctuation,  $I/\Delta I$ , is  $\sim 30$ . Furthermore, Zemcov et al. (2014) find excellent spatial correlation among 1.1, 1.6 and Spitzer 3.6  $\mu\text{m}$ . Since no clear signature of redshifted Lyman  $\alpha$  is detected, they conclude that the first stars are not the source of excess fluctuation. They also exclude direct-collapsed black holes (DCBHs) model (Yue et al. 2013b), since the detected fluctuation is too high and the color is quite different from the prediction. Zemcov et al. (2014) claim that the large portion of the observed fluctuation can be explained with intra halo light (IHL) and estimate the surface brightness of IHL to be comparable to that of ILG. It must be emphasized that the quoted EBL (ILG plus IHL) is still a few times lower than that of the residual emission obtained in this work.

At present, there is no definite emission source which can explain the observed excess brightness. More observational and theoretical work is needed to delineate the emission source of excess brightness and fluctuation.

## 6. Summary

The reanalysis of the IRTS data was performed to obtain improved and more reliable measurement of the near-infrared residual isotropic emission. We revised the estimation of the integrated star light due to faint unresolved stars and the thermal emission part of the zodiacal light spectrum. We take the diffuse Galactic light into account based on the recent observations with AKARI and CIBER. Besides the Kelsall model for the zodiacal light used in paper I, another model, the Wright model, was examined, too.

The result for the Kelsall model shows peak value of  $60 \text{ nWm}^{-2}\text{sr}^{-1}$  which is  $\sim 11 \text{ nWm}^{-2}\text{sr}^{-1}$  lower than that of paper I. This is still considerably brighter than the integrated light of galaxies (ILG). The result for the Wright model shows peak value of 53

$\text{nWm}^{-2}\text{sr}^{-1}$  which is slightly fainter than that of the Kelsall model. Both models render significant residual isotropic emission that cannot be explained with known foreground emission sources.

## 7. ACKNOWLEDGMENTS

The authors thank Shuji Matsuura and Toshiaki Arai for their encouragement and valuable comments. Thanks are also due to Edward L. Wright for his courtesy in providing the code of his zodiacal light model. K.T. was supported by KAKENHI (26800112) from JSPS, Japan.

This publication makes use of data products from the Two Micron All Sky Survey, which is a joint project of the University of Massachusetts and the Infrared Processing and Analysis Center/California Institute of Technology, funded by the National Aeronautics and Space Administration and the National Science Foundation.

## REFERENCES

- Arai, T. et al. 2015, ApJ, accepted (arXiv:1503.04926)
- Bernstein, R. A. 2007, ApJ, 666, 663
- Brandt, T. D., & Draine, B. T. 2012, ApJ, 744, 129
- Cambr  sy, L., Reach, W. T., Beichman, V. A. & Jarrett, T. H. 2001, ApJ, 555, 563
- Cohen, M. 1997, ASP Conf. Series, 124, Diffuse Infrared Radiation and the IRTS eds. H. Okuda, T. Matsumoto & T. Roellig, 61
- Cooray, A. et al. 2012, Nature, 490, 514
- Cooray, A. et al. 2012, ApJ, 756, 92
- Dwek, E., Arendt, R. G., & Krennrich, F. 2005, ApJ, 635, 784
- Girardi, L., Gronewegen, M. A., Hatziminaglou, E. & Costa, D. da 2005, A&A, 436, 895
- Gorjian, V. Wright, E. & Chary, R. R. 2000 ApJ, 536, 550
- Hanner, M. S. et al. 1974, J. Geophys. Res., 79, 3671
- Kashlinsky, A., Arendt, R. G., Mather, J., & Moseley, S. H. 2005, Nature, 438, 45
- Kashlinsky, A., Arendt, R. G., Mather, J., & Moseley, S. H. 2007a, ApJ, 654, L5
- Kashlinsky, A., Arendt, R. G., Mather, J., & Moseley, S. H. 2007b, ApJ, 666, L1
- Kashlinsky, A. et al. 2012, ApJ, 753, 63
- Keenan, R. C., Barger A. J., Cowie L. L., & Wang, W. -H. 2010, ApJ, 723, 40
- Kelsall, T., et al. 1998, ApJ, 508, 44



- Levenson, L. R., Wright, E. L. & Johnson, B. D. 2007, ApJ, 666, 34
- Matsumoto, T., et al. 2011, ApJ, 742, 124 (paper I)
- Matsumoto, T., et al. 2005, ApJ, 626, 31
- Mattila, K. 2006, MNRAS, 372, 1253
- Mattila, K., et al. 2011, Proceedings IAU Symoisium No. 284, 429
- Murakami, H. et al. 1996, PASJ, 48, L41
- Matsuoka, Y., Ienaka, N., Kawara, K. & Oyabu, S. 2011, ApJ, 736, 119
- Noda, M. et al. 1994, ApJ, 428, 363
- Noda, M. et al. 1996, SPIE, 2817, 248
- Seo, H. J. et al. 2014, ApJ, accepted (arXiv:1504.05681)
- Schlegel, D. J., Finkbeiner, D. P., & Davis, M. 1998, ApJ, 500, 525
- Skrutskie, M. ,F. 2006, AJ, 131, 1163
- Pyo, J., Matsumoto, T., Jeong, W. S. & Matsuura, S. 2012, ApJ, 760, 102
- Totani,T. & Yoshii, Y. 2000, ApJ, 540, 81
- Tsumura, K. et al. 2010, ApJS, 719, 394
- Tsumura, K. et al. 2013a, ApJS, 207, 33
- Tsumura, K., Matsumoto, T., Matsuura, S., Sakon, I., Pyo, J. & Wada, T. 2013b, PASJ, 65, 119
- Tsumura, K., Matsumoto, T., Matsuura, S., Sakon, I., Tanaka, M. & Wada, T. 2013c, PASJ, 65, 120

Tsumura, K., Matsumoto, T., Matsuura, S., Sakon, I., & Wada, T. 2013d, PASJ, 65, 121

Wright, E. 1998, ApJ, 496, 1

Wright, E. L. & Reese, E. D. 2000, ApJ, 545, 43

Yue, et al. 2013, MNRAS, 431, 383

Yue, et al. 2013, MNRAS, 433, 1556

Zemcov, M. et al. 2013, ApJS, 207, 31

Zemcov, M. et al. 2014, Science, 346, 732

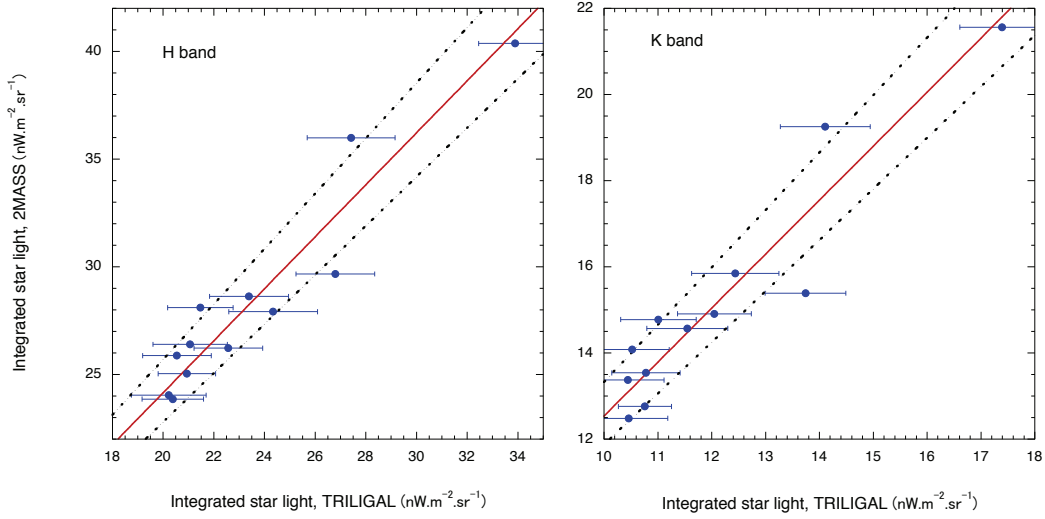


Fig. 1.— The correlation between the TRILEGAL ISL (the integrated light for stars fainter than the IRTS limiting magnitude based on the TRILEGAL Galaxy model) and the 2MASS ISL (the integrated light for 2MASS stars fainter than IRTS limiting magnitude and for stars fainter than 2MASS limiting magnitude based on the TRILEGAL Galaxy model) for the 12 selected IRTS fields. Left and right panels show the case for the H and K band, respectively. Horizontal error bars represent the standard deviation of the TRILEGAL ISL which was obtained using Monte Carlo simulations. Straight lines show the best fit for linear correlation, and the dotted lines indicate the adopted  $\pm 1\sigma$  error.

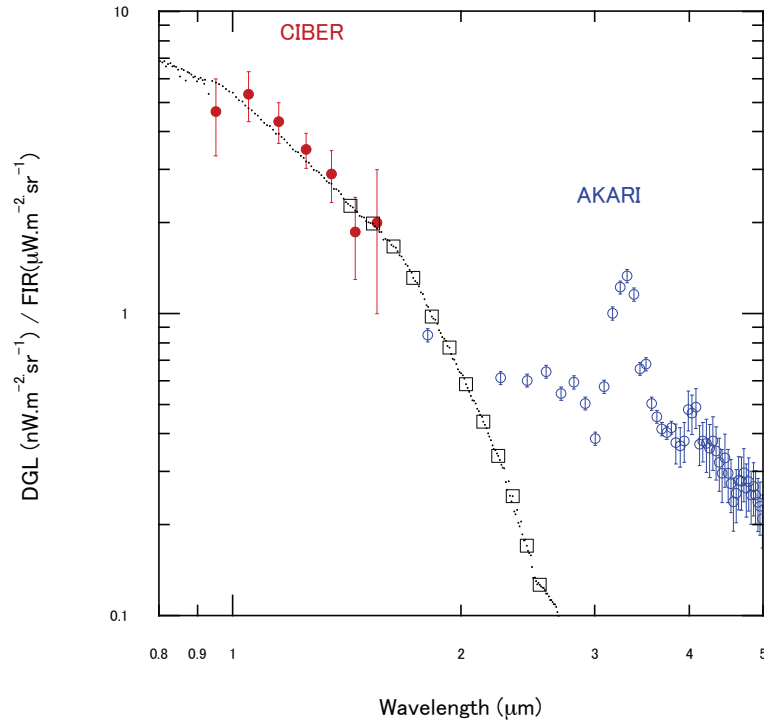


Fig. 2.— The ratio of the DGL to the far-infrared ( $100 \mu\text{m}$ ) emission, shown in units of  $\text{nWm}^{-2}\text{sr}^{-1}$  (DGL)/  $\mu\text{Wm}^{-2}\text{sr}^{-1}$  (FIR). Filled and open circles represent the result of CIBER (Arai et al. 2015) and AKARI (Tsumura et al. 2013c), respectively. Dotted line shows the model (ZDA04-BC03 in Brandt and Draine (2012)) recommended by Arai et al. (2015), and open squares indicate adopted ratio for IRTS bands.

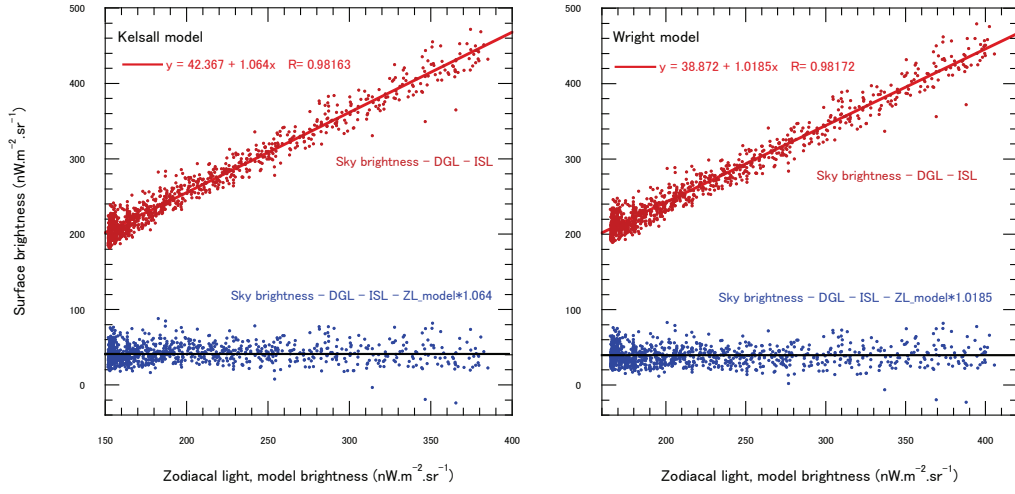


Fig. 3.— Upper set of data points shows the correlation diagram between the surface brightness after subtracting ISL and DGL from observed sky brightness at  $1.8 \mu\text{m}$ , and model ZL brightness. Left and right panels indicate the case for the Kelsall and Wright model, respectively. Solid lines are best fit lines for linear correlation. Lower set of data points represents individual residual emission after subtracting all foreground emission from observed sky brightness in which solid lines show residual emission obtained by linear correlation analysis.

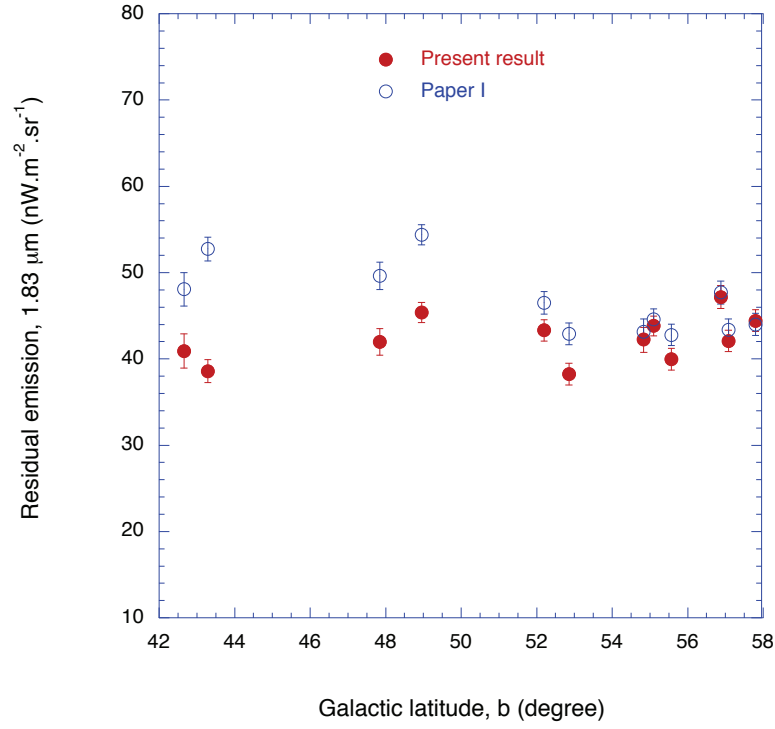


Fig. 4.— Dependence of residual emission at  $1.8 \mu\text{m}$  on the Galactic latitudes for the case of the Kelsall model. Filled circles and open circles represent the result of this work and that of paper I, respectively. Data are taken by averaging individual residuals for 10 degrees along Galactic longitude.

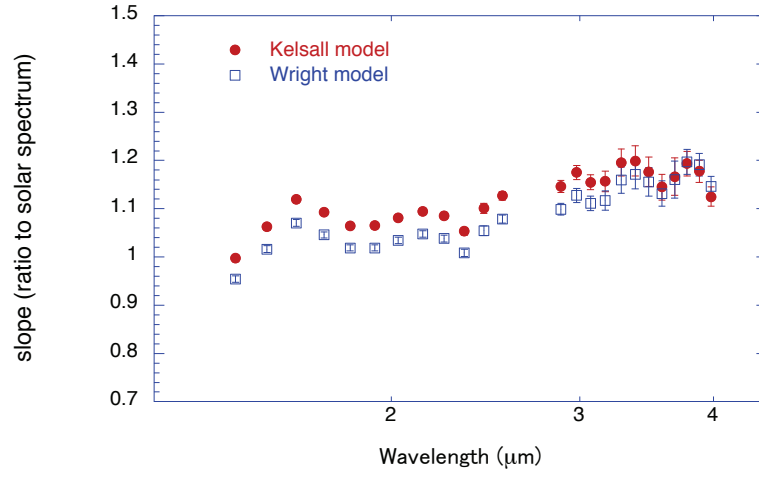


Fig. 5.— Wavelength dependence of the slopes of the linear fit lines in the upper part of Fig.3. Slopes represent ratios to the solar spectrum. Filled and open circles represent the case for the Kelsall model and the Wright model, respectively.

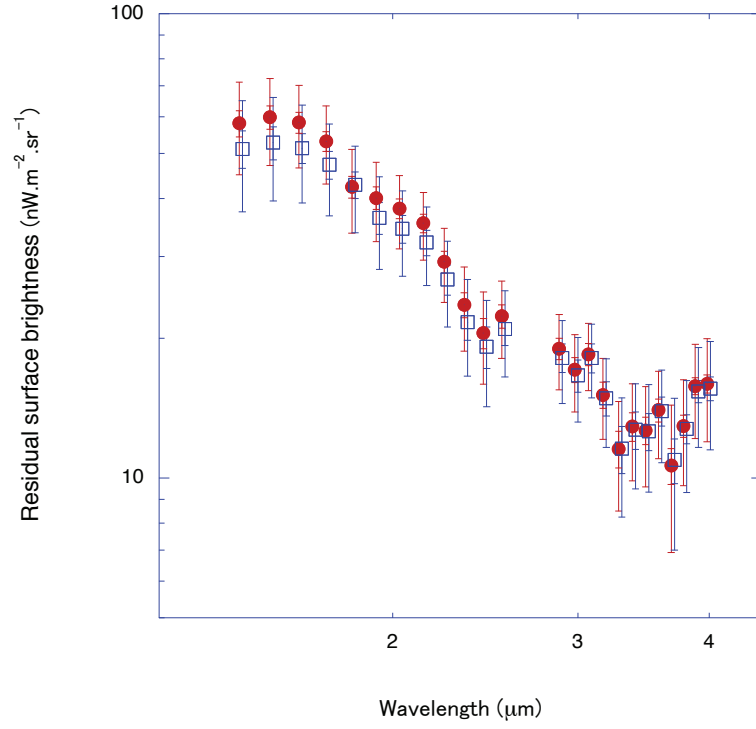


Fig. 6.— Spectra of residual isotropic emission after subtracting ZL, DGL and ISL are shown for the Kelsall (filled circles) and the Wright model (open squares), respectively. For clarity, the residual emission of the Wright model is shifted to slightly longer wavelength. Two sets of error bars are plotted for each data point. The inner bars represent random errors, while the outer bars indicate the total error including systematic errors.



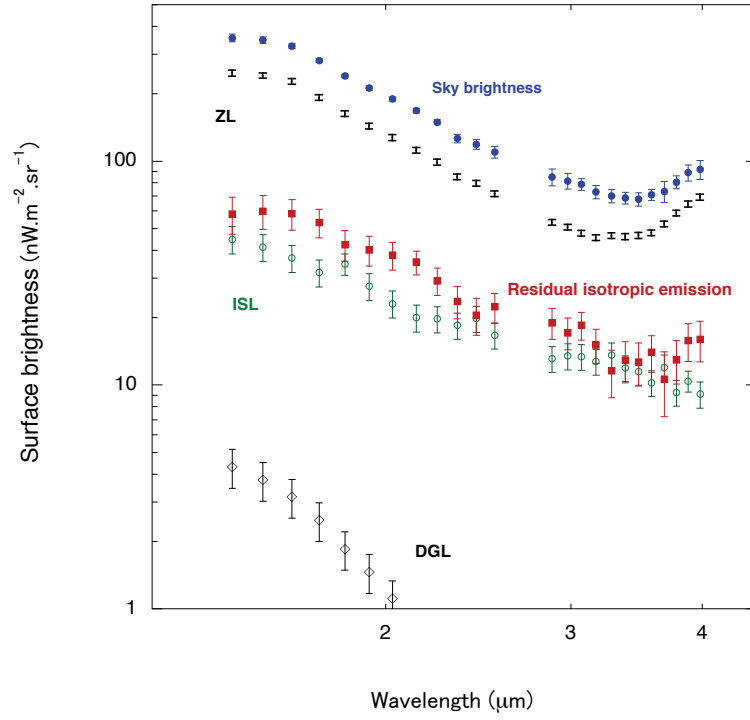


Fig. 7.— A breakdown of the sky brightness at high ecliptic latitudes ( $\beta > 70^\circ$ ) and high Galactic latitude ( $b > 45^\circ$ ) for the case of the Kelsall model. Filled circles, bars, filled squares, open circles, and open diamonds indicate the observed sky brightness, zodiacal light (ZL), residual isotropic emission, integrated star light (ISL) and diffuse Galactic light (DGL), respectively.

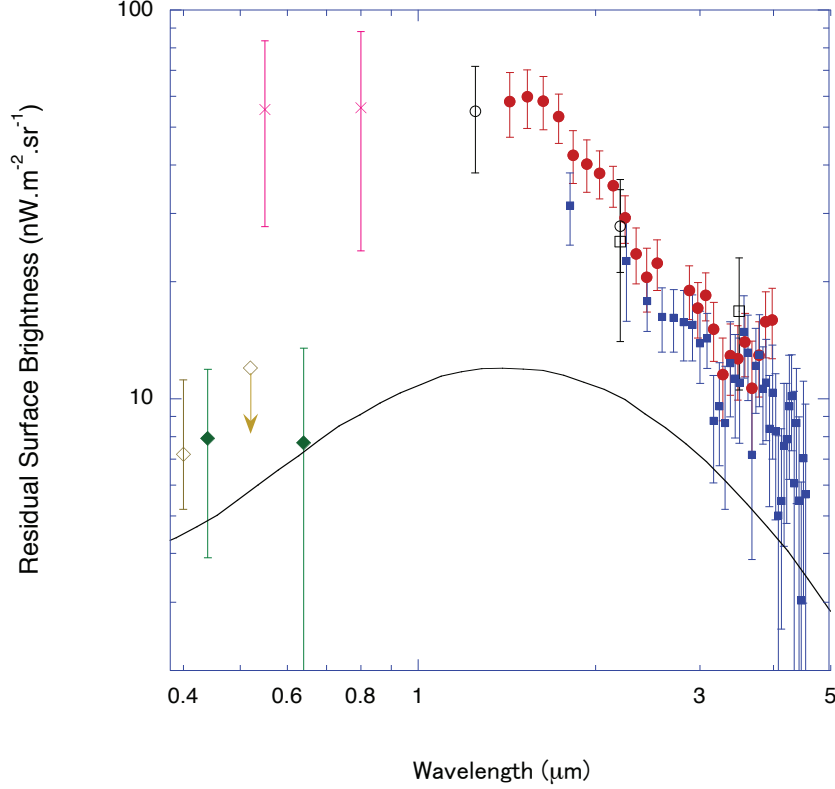


Fig. 8.— Summary of observations of the residual isotropic emission for the case of the Kelsall model. Symbols represent following data: filled circles (IRTS, this work), filled squares (AKARI, Tsumura et al. (2013d)), open circles (COBE, Cambr sy et al. (2001)), open squares (COBE, Levenson et al. (2007)), crosses (HST, Bernstein (2007)), filled diamonds (Pioneer 10/11, Matsuoka et al. (2011)), and open diamonds (dark cloud, Mattila et al. (2011)). The solid line shows the integrated light of galaxies (ILG) (Totani and Yoshii 2000).

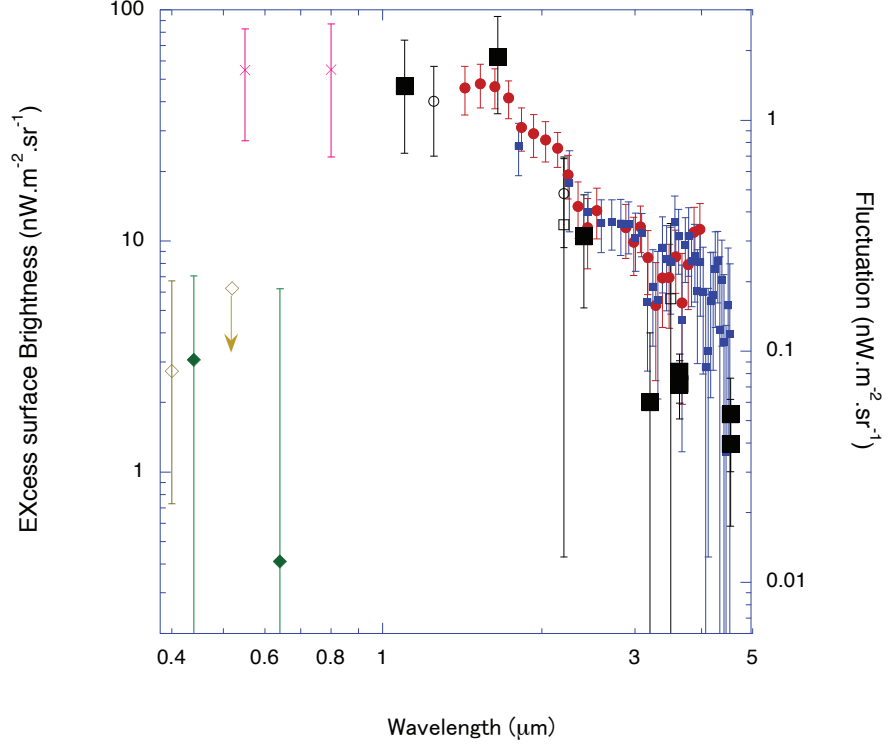


Fig. 9.— Summary of the excess emission over integrated light of galaxies (ILG). Symbols represent the following data: filled circles (IRTS, this work), filled squares (AKARI, Tsumura et al. (2013d)), open circles (COBE, Cambr  sy et al. (2001)), open squares (COBE, Levenson et al. (2007)), crosses (HST, Bernstein (2007)), filled diamonds (Pioneer 10/11, Matsuoka et al. (2011)), and open diamonds (dark cloud, Mattila et al. (2011)). Large filled squares indicate fluctuations of the sky observed with Spitzer, AKARI and CIBER (Zemcov et al. 2014) with the right ordinate having the same dynamic range as the excess brightness.

Table 1: Surface brightness of residual isotropic emission and its errors in units of  $\text{nWm}^{-2}\text{sr}^{-1}$

Wavelength [ $\mu\text{m}$ ]	Kelsall		Wright	
	Residual	Total Error	Residual	Total Error
3.98	16.0	4.0	15.6	4.1
3.88	15.8	3.6	15.4	3.7
3.78	12.9	3.3	12.8	3.4
3.68	10.6	3.7	10.9	3.9
3.58	14.0	3.0	13.9	3.1
3.48	12.7	3.1	12.6	3.3
3.38	12.9	3.0	12.7	3.2
3.28	11.6	3.1	11.6	3.3
3.17	15.1	3.0	14.9	3.2
3.07	18.5	3.0	18.2	3.3
2.98	17.1	3.2	16.6	3.4
2.88	19.0	3.5	18.2	3.7
2.54	22.3	4.2	20.9	4.4
2.44	20.5	4.6	19.2	4.9
2.34	23.6	4.9	21.7	5.1
2.24	29.2	5.3	26.8	5.6
2.14	35.4	5.9	32.2	6.2
2.03	38.0	6.8	34.4	7.2
1.93	40.1	7.8	36.3	8.2
1.83	42.4	8.7	42.8	9.0
1.73	53.1	10.1	47.3	10.6
1.63	58.3	11.8	51.4	12.2
1.53	59.9	12.7	52.8	13.3
1.43	58.1	13.1	51.2	13.7